Detectability of patches in fractal textures for assessing Hölder exponent-based breast cancer risk evaluation

Barbara Pascal, Hermine Biermé

▶ **To cite this version:**

Barbara Pascal, Hermine Biermé. Detectability of patches in fractal textures for assessing Hölder exponent-based breast cancer risk evaluation. 2025. hal-04953522

HAL Id: hal-04953522
https://hal.science/hal-04953522v1

Preprint submitted on 18 Feb 2025

HAL is a multi-disciplinary open access archive for the deposit and dissemination of scientific research documents, whether they are published or not. The documents may come from teaching and research institutions in France or abroad, or from public or private research centers.

L'archive ouverte pluridisciplinaire **HAL**, est destinée au dépôt et à la diffusion de documents scientifiques de niveau recherche, publiés ou non, émanant des établissements d'enseignement et de recherche français ou étrangers, des laboratoires publics ou privés.

Distributed under a Creative Commons Attribution 4.0 International License

Detectability of patches in fractal textures for assessing Hölder exponent-based breast cancer risk evaluation

Barbara Pascal
Nantes Université, École Centrale Nantes
CNRS, LS2N, UMR 6004, F-44000 Nantes, France
barbara.pascal@cnrs.fr

Hermine Biermé
Université de Tours
CNRS, UMR 7013, Institut Denis Poisson, France
hermine.bierme@univ-tours.fr

***Abstract*—Early detection of breast cancer is key to patient's survival. Recent works showed that the distribution of local Hölder exponents in a mammogram can quantify breast tissue disruption, and hence assess breast cancer risk. This work proposes a systematic study of the detectability of disrupted tissues embedded inside either fatty or dense tissues leveraging simulated piecewise homogeneous fractal textures modeling the breast tissues. A novel filtered fractional Brownian field model for stationary isotropic fractal textures is proposed, based on a genuinely designed isotropic filtering. Intensive simulations on synthetic textures generated either from the previously introduced fractional Gaussian field or from the novel filtered fractional Brownian field show that a state-of-the-art local Hölder exponent-based segmentation algorithm is capable of detecting large patches of disrupted tissues in fatty environments, but that segmentation accuracy drops down for small patches, while for dense environments performance are good and decrease slowly with the patch size.**

***Index Terms*—Breast cancer, Fractal textures, Brownian fields, Texture segmentation, Detectability, Multiscale analysis, Variational estimator.**

I. Introduction

Context. Breast cancer is the most represented cancer among women worldwide. According to the Canadian[1] and American[2] Cancer Societies up to one woman over eight will be diagnosed with a breast cancer during her lifetime, and one over thirty-four will die from it. Furthermore, autopsy surveys found a large number of occult cancerous breast tumors [1], [2] which remained undetected. Yet, early and efficient detection is critical to the patient's survival [3]. Hence, massive research efforts have been made to enable breast cancer detection at early stages [4]. The main diagnostic tool consists in X-ray examination, though the resulting *mammography* turns out to be rather difficult to interpret precisely for radiologists as normal tissues might have very different appearance across the breast [5].

Related works. Fractal tools have been applied to analyze a large variety of medical images and proved efficient in many diverse tasks, from characterization of osteoporosis in X-ray images of bones [6]–[9], to morphological evaluation of white matter in magnetic resonance images of the brain [10]. To name but a few, the fractal dimension of the rough surface associated to a gray-scale image has been successfully used for segmentation of ultrasound images [11] and for characterizing the breast density [12] and turned out capable to contribute to breast cancer risk assessment [12]. Detection of potentially cancerous lesions in the breast has been addressed in several ways: for example based on the power-law exponent of Fourier spectrum [13]. Using an a contrario framework designed for the detection of spots in textures backgrounds, the ability to identify lesions in mammograms has been quantified systematically [14]. Recently, local measures of the self-similarity index in mammograms, through their so-called *local Hölder exponent*, have been leveraged to yield very accurate cancer detection [15] and cancer risk assessment [4], [16]. Beyond medical imaging, it is worth noting that detectability has also been quantified in a multifractal framework [17] in which homogeneous textures are characterized by a *distribution* of spatially varying Hölder regularity instead of by a fixed value.

Goals, contributions and outline. Following the numerous works modeling breast tissues as fractal textures [4], [5], [12], [16], the present work aims at quantifying the detectability of patches of disrupted tissues, modeled by fractal textures of Hölder exponent $H_{\mathrm{p}} = 0.5$ [4], [16], immersed either in fatty or dense microenvironments, modeled as fractal textures of respective Hölder exponents $H_{\mathrm{b}} = 0.3$ or $H_{\mathrm{b}} = 0.65$ [4], [5], [16]. In particular, the influence of the both the relative and absolute patch size on segmentation accuracy is investigated. To that aim a synthetic framework designed to mimic closely real mammograms is leveraged to provide quantitative detection performance. Two models of self-similar textures characterized by an homogeneous local Hölder exponent are recalled in Section II and a novel model based on a recently developed undecimated isotropic filtering is proposed, enabling an even better match with real textures and thus contributing to breast tissue modeling. Section III recalls the principles of multiscale analysis for local Hölder exponent estimation and sketches the automated data-driven Threshold-ROF variational estimator of the local regularity used to perform texture segmentation. Section IV introduces a novel framework for detectability assessment and presents intensive Monte Carlo numerical experiments characterizing the detectability of a patch of disrupted tissue embedded in fatty or dense tissues.

II. Piecewise homogeneous fractal textures

Modeling and simulation of fractal textures has triggered intense research efforts from both the stochastic geometry and computer vision communities [18]–[20] and beyond [21]. From a mathematical perspective, a gray-scale image can be modeled by a real-valued field $\mathsf{F} : \mathbb{R}^2 \to \mathbb{R}$. Textured images are well-described by *random* fields. In particular, natural images, e.g., biomedical images [4], [5], [22], are appropriately modeled by self-similar Gaussian fields [20] satisfying

$$\forall c > 0, \quad \{\mathsf{F}(c\underline{x}); \underline{x} \in \mathbb{R}^2\} \overset{(law)}{=} c^H \{\mathsf{F}(\underline{x}); \underline{x} \in \mathbb{R}^2\} \tag{1}$$

for some self-similarity index $H \in (0, 1)$.

Isotropic self-similar fields. The *fractional Brownian field* of parameter $H \in (0, 1)$, denoted by B_H, is a very standard model of self-similar Gaussian field [23]. It has the harmonizable representation:

$$\mathsf{B}_H(\underline{x}) = \int_{\mathbb{R}^2} \frac{\mathrm{e}^{-\mathrm{i}\underline{x}\cdot\underline{\omega}} - 1}{\|\underline{\omega}\|^{H+1}} \, \mathrm{d}\widetilde{\mathsf{G}}(\underline{\omega}) \tag{2}$$

where $\underline{x}\cdot\underline{\omega} = x_1\omega_1 + x_2\omega_2$ denotes the Euclidean product in $\mathbb{R}^2$ and $\|\underline{\omega}\| = \sqrt{\omega_1^2 + \omega_2^2}$ the associated norm and $\widetilde{\mathsf{G}}$ referred to the Fourier

Work partly supported by ANR-19-CE40-0005 "*MISTIC*".

[1] https://cancer.ca/en/research/cancer-statistics

[2] https://www.cancer.org/cancer/types/breast-cancer.html

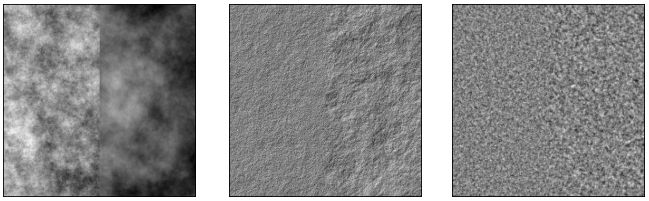

(a) fBf [20], see (2) (b) fGf [24], see (4) (c) Filtered fBf (5)

Fig. 1: **Piecewise homogeneous fractal textures.** Three models of self-similar textures characterized by their Hurst exponent are compared. Each image is composed, on the left half, of an homogeneous textures with Hurst exponent $H = 0.3$, on the right half, of an an homogeneous texture of Hurst exponent $H = 0.65$.

transform of a two-dimensional Wiener process. From Equation (2), it can be shown that B_H satisfies the self-similarity condition (1) and that its covariance function writes for any $\underline{x}, \underline{y} \in \mathbb{R}^2$:

$$\mathbb{E}\left[\mathsf{B}_H(\underline{x})\mathsf{B}_H(\underline{y})\right] = \frac{1}{2}\left(\|\underline{x}\|^{2H} + \|\underline{y}\|^{2H} - \|\underline{x}-\underline{y}\|^{2H}\right) \quad (3)$$

where $\|\underline{x}\|^2 = x_1^2 + x_2^2$ denotes the squared Euclidean norm. As can be seen on the covariance function (3), fractional Brownian fields, although isotropic, are not stationary: the variance of the field B_H at point $\underline{x}$ depends on the distance to the origin $\|\underline{x}\|$. Figure 1a shows the juxtaposition of two fractional Brownian fields of respective parameters $H = 0.3$ (left) and $H = 0.65$ (right); the nonstationarity makes the frontier between the two textures discontinuous, which is not appropriate for modeling neighboring breast tissues. Instead, to account for the visual continuity required when it comes to mimic real-world images, *stationary* texture models have been considered [24]. For a self-similarity index $H \in (0,1)$, the *fractional Gaussian field* G_H introduced in [24] is defined as the sum of horizontal vertical increments of the fractional Brownian field

$$\mathsf{G}_H(\underline{x}) = \frac{1}{2}\left(\mathsf{B}_H(\underline{x}+\underline{e}_1) + \mathsf{B}_H(\underline{x}+\underline{e}_2) - 2\mathsf{B}_H(\underline{x})\right) \quad (4)$$

where $\underline{e}_1 = (1,0)$ and $\underline{e}_2 = (0,1)$. As shown in [24, Proposition 4], G_H is an isotropic, stationary and asymptotically self-similar Gaussian field, which translates in Figure 1b into a far more realistic frontier between the two different textures. Though, the choice of horizontal and vertical directions might appear arbitrary, motivating the construction of a generalization of the fractional Gaussian field (4) including *all* directions. The novel isotropic stationary fractal texture model consists in a isotropic filtering of the fractional Brownian field (2) inspired by the monogenic wavelet transform introduced in [25]. The *filtered fractional Brownian field* is defined as

$$\mathsf{C}_H(\underline{x}) = \langle \mathsf{B}_H, \mathsf{u}_{\underline{x}} \rangle, \quad (5)$$

with a smooth radial function u satisfying $\int_{\mathbb{R}^2} \mathsf{u}(\underline{x})d\underline{x} = 0$ given by the high-pass filter proposed in [25, Section 4.2] at scale 2^3, which balances self-similarity preservation and visual aspect. As observed in Figure 1c, the border between the two textures is almost invisible.

Synthesis of piecewise homogeneous textures. To quantify the detectability of patches of disrupted tissues, corresponding to fractal fields of self-similiarity index $H_\mathrm{p} = 0.5$, immersed in fatty tissues, corresponding to a background texture characterized by $H_\mathrm{b} = 0.3$, or in dense tissues, corresponding to $H_\mathrm{b} = 0.65$, synthetic *piecewise* homogeneous fractal textures are required. To that aim, an image is considered as the restriction of a field to a square domain Ω and, as illustrated in the fist column of Figure 2, a partition $\Omega = \Omega_\mathrm{p} \cup \Omega_\mathrm{b}$, $\Omega_\mathrm{p} \cap \Omega_\mathrm{b} = \emptyset$ is built where Ω_p consists in a central disk modeling the

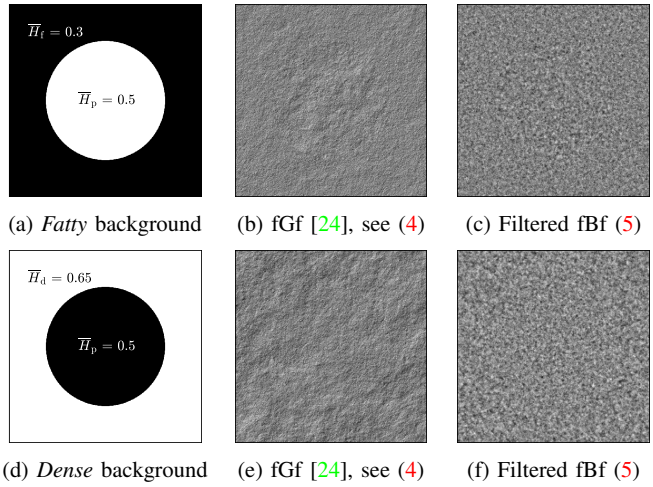

(a) *Fatty* background (b) fGf [24], see (4) (c) Filtered fBf (5)

(d) *Dense* background (e) fGf [24], see (4) (f) Filtered fBf (5)

Fig. 2: **Piecewise homogeneous fractional Gaussian vs. filtered fractional Brownian fields.** The central patch to be detected covers 30% of the total image which is of resolution 512×512 pixels. First row: detection of disrupted tissues in a *fatty* background. Second row: detection of disrupted tissues in a *dense* background;

patch to be detected and Ω_b corresponds to the background. On each domain, independent homogeneous textures of corresponding self-similarity index are generated, leading to a piecewise homogeneous one, examples of which are provided in the second and third columns of Figure 2 using respectively the fractional Gaussian field (4) and the filtered fractional Brownian field (5) models. The first row of Figure 2 models a patch of disrupted tissue in a fatty environment, while the second row mimics disrupted tissues in a dense environment.

III. Hölder exponent-based texture segmentation

The local self-similarity index in mammograms is measured through their *local Hölder exponent* [4], [15], [16] as the two notions coincide for numerous fractal texture models, notably for the fractional Brownian field (2), the fractional Gaussian field (4) and the novel filtered fractional Brownian field (5).

Self-similarity and local Hölder exponent. At a point $\underline{x}_0 \in \Omega$, the *local Hölder exponent* of a field $\mathsf{F} : \mathbb{R}^2 \to \mathbb{R}$, denoted $h(\underline{x}_0)$, is defined as the largest exponent $\alpha > 0$ such that there exist a constant χ and a polynomial $\mathcal{P}_{\underline{x}_0}$ of degree lower than α such that for $\underline{x}$ in a neighborhood of $\underline{x}_0$: $|\mathsf{F}(x) - \mathcal{P}_{\underline{x}_0}(\underline{x})| \leq \chi\|\underline{x} - \underline{x}_0\|^\alpha$. The local Hölder exponent of the fields B_H, G and C_H defined in Equations (2), (4) and (5) is constant equal to H, i.e., $\forall \underline{x} \in \mathbb{R}^2$, $h(\underline{x}) = H$.

Multiscale analysis and wavelet leaders. As the local Hölder exponent is deeply linked to self-similarity, a natural estimation framework is multiscale analysis. Let ϕ and ψ referring respectively to the scaling function and to the mother wavelet, characterized by its number of vanishing moment N_ψ,defining a one-dimensional multiscale analysis provided that $N_\psi \geq 1$ [26]. Then, the two-dimensional wavelets, depending on $\underline{x} = (x_1, x_2) \in \mathbb{R}^2$, are defined from ϕ and ψ as

$$\begin{cases} \psi^{(0)}(\underline{x}) = \phi(x_1)\phi(x_2), & \psi^{(1)}(\underline{x}) = \psi(x_1)\phi(x_2) \\ \psi^{(2)}(\underline{x}) = \phi(x_1)\psi(x_2), & \psi^{(3)}(\underline{x}) = \psi(x_1)\psi(x_2). \end{cases} \quad (6)$$

The two-dimensional wavelet coefficients of a (random) field $\mathsf{F} : \Omega \subseteq \mathbb{R}^2 \to \mathbb{R}$ are then defined as $Y_\mathsf{F}^{(m)}(j,\underline{k}) = 2^{-j}\langle \mathsf{F}, \psi_{j,\underline{k}}^{(m)} \rangle$ where j is the octave, linked to the scale $a = 2^j$, $\underline{k} = 2^{-j}\underline{x}$ is the location on the dyadic lattice, $m \in \{0,1,2,3\}$ is the direction and $\psi_{j,\underline{k}}^{(m)}$ correspond to the m wavelet $\psi^{(m)}$ dilated to scale $a = 2^j$ and translated to

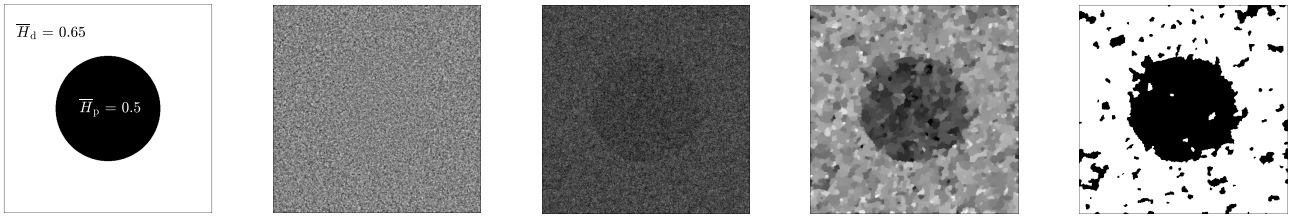

(a) True $\overline{\boldsymbol{h}}$ (b) Piecewise texture (c) Lin. reg. $\widehat{\boldsymbol{h}}^{\mathsf{LR}}$ (d) ROF $\widehat{\boldsymbol{h}}^{\mathsf{ROF}}$ (e) T-ROF $\mathcal{T}\widehat{\boldsymbol{h}}^{\mathsf{ROF}}$

Fig. 3: **Automated data-driven local Hölder exponent-based texture segmentation.** Segmentation of a central patch covering 20% of an $N \times N$ pixels image consisting in a filtered fractional Brownian field of self-similarity index $\overline{H}_{\mathrm{p}} = 0.5$ plunged into a fractional Gaussian field of self-similarity index $\overline{H}_{\mathrm{d}} = 0.65$ with $N = 512$. (a) Ground truth local Hölder exponent map $\overline{\boldsymbol{h}}$. (b) Piecewise homogeneous fractal texture $\underline{x}$. (c) Linear regression estimate of the local Hölder exponent $\widehat{\boldsymbol{h}}^{\mathsf{LR}}$. (d) Regularized estimate $\widehat{\boldsymbol{h}}^{\mathsf{ROF}}$ obtained from (9) with automated selection of the regularization parameter through minimization of (10). (e) Segmentation after iterative thresholding achieving $\mathsf{F}_1 = 0.94$.

location $\underline{x} = 2^j \underline{k}$. The factor 2^{-j} enforces the L^1 normalization of the wavelet transform. If furthermore, the wavelet ψ has compact support, then the wavelet leader coefficients $\mathcal{L}_{j,\underline{k}}$, at scale 2^j and location $\underline{x} = 2^j \underline{k}$, are defined as the local supremum of modulus of wavelet coefficients in a small neighborhood across all finer scales $j' \leq j$ [27]–[29]

$$\mathcal{L}_{j,\underline{k}} = \sup_{\substack{\lambda_{j',\underline{k}'} \subset 3\lambda_{j,\underline{k}} \\ m \in \{1,2,3\}}} |2^j d^{(m)}_{j',\underline{k}'}|, \tag{7}$$

with $\lambda_{j,\underline{k}} = [\underline{k}2^j, (\underline{k}+1)2^j)$ and $3\lambda_{j,\underline{k}} = \bigcup_{\underline{p} \in \{-1,0,1\}^2} \lambda_{j,\underline{k}+\underline{p}}$ [27]–[29]. As demonstrated in [27], [30], under mild regularity conditions on F

$$\mathcal{L}_{j,\underline{k}} \simeq \eta(\underline{x}) 2^{j h(\underline{x})} \quad \text{as} \quad 2^j \to 0, \tag{8}$$

at $\underline{x} = 2^j \underline{k}$ and where $\eta(\underline{x}) > 0$ does not depend on j. Hence, the local Hölder exponent at location $\underline{x}$ can be obtained by performing a linear regression of $\log_2 \mathcal{L}_{j,\underline{k}}$ across small scales while keeping $\underline{k} = 2^{-j}\underline{x}$ from octave $j_{\min} = 1$ to $j_{\max} = 3$, which is a compromise between accuracy of the estimate and locality required when performing a segmentation. Figure 3c shows the pixelwise linear regression estimate of the local Hölder exponent of the piecewise homogeneous texture of Figure 3b. It appears far too noisy to perform an accurate segmentation, hence requiring a posteriori regularization.

Threshold-ROF estimator. For a textured image composed of $M = N \times N$ pixels, let $\boldsymbol{h}^{\mathsf{LR}} \in \mathbb{R}^M$ denote the pixelwise linear regression estimates of its local Hölder exponent stored in a vector form. The regularized ROF estimate of the local Hölder exponent, originally proposed in [31] and then reframed using the wavelet leader formalism in [24], [32], is built as the minimizer of an objective function composed of a data-fidelity term and a Total Variation penalization, which favors piecewise constancy and hence accurate segmentation. It writes

$$\widehat{\boldsymbol{h}}^{\mathsf{ROF}} = \operatorname*{argmin}_{\boldsymbol{h} \in \mathbb{R}^M} \|\boldsymbol{h} - \widehat{\boldsymbol{h}}^{\mathsf{LR}}\|_2^2 + \lambda \|\mathbf{D}\boldsymbol{h}\|_{2,1} \tag{9}$$

where $\|\cdot\|_2$ denotes the Euclidean norm in $\mathbb{R}^M$, $\mathbf{D} : \mathbb{R}^M \to \mathbb{R}^{2\times M}$ is the two-dimensional discrete gradient operator and $\|\cdot\|_{2,1}$ in the mixed 2, 1-norm in $\mathbb{R}^{2\times M}$. The objective function minimized in (9) is strongly-convex, due to the square ℓ_2, norm but nonsmooth, because of the mixed $\ell_{2,1}$-norm involved in the isotropic Total Variation penalization. Hence, minimizing (9) requires to resort to proximal algorithms. In this work, an accelerated Chambolle-Pock primal-dual scheme [33] particularized to fractal texture segmentation in [34, Algorithm 1] yields a fast scheme to compute $\widehat{\boldsymbol{h}}^{\mathsf{ROF}}$ which scales up to large size images with $N \gtrsim 1024$. As illustrated in Figure 3d the resulting estimate of local Hölder exponent resembles far more the ground truth of Figure 3a. Furthermore, applying the short iterative thresholding post-processing proposed in [35] leads to the segmentation denoted $\mathcal{T}\widehat{\boldsymbol{h}}^{\mathsf{ROF}}$ shown in Figure 3e which is very satisfactory given the difficulty of the task.

Stein-based automated parameter tuning. In Equation (9), the regularization parameter λ plays a paramount role in achieving accurate segmentation. In the present work, this hyperparameter is thus fine-tuned using the flexible automated and data-driven procedure proposed in [34], [36], which consists in the minimization of a genuinely designed Generalized Stein Unbiased Risk Estimate

$$\mathsf{GSURE}(\lambda) = \left\|\widehat{\boldsymbol{h}}^{\mathsf{ROF}} - \widehat{\boldsymbol{h}}^{\mathsf{LR}}\right\|^2 + 2\mathrm{Tr}\left(\boldsymbol{\mathcal{S}}\boldsymbol{J}\right) - \mathrm{Tr}(\boldsymbol{\mathcal{S}}) \tag{10}$$

where $\boldsymbol{\mathcal{S}} \in \mathbb{R}^{M\times M}$ is the covariance matrix of the additive Gaussian noise corrupting the linear regression estimate and $\boldsymbol{J} \in \mathbb{R}^{M\times M}$ is the Jacobian matrix of $\widehat{\boldsymbol{h}}^{\mathsf{ROF}}$ with respect to $\widehat{\boldsymbol{h}}^{\mathsf{LR}}$. As $\widehat{\boldsymbol{h}}^{\mathsf{LR}}$ presents significant spatial correlations arising from self-similarity and from the multiscale framework used for estimation, $\boldsymbol{\mathcal{S}}$ is non-trivial. Though, assuming that the correlation length is bounded by the largest scale $2^{j_{\max}}$ considered, $\boldsymbol{\mathcal{S}}$ can be estimated in a data-driven manner with good accuracy, following [34], [36]. Finally, the minimization of (10) is performed efficiently leveraging Broyden-Fletcher-Goldfarb-Shanno algorithm [36, Algorithm 3].

IV. Detectability assessment

Intensive Monte Carlo numerical experiments are conducted to assess the ability of the automated data-driven texture segmentation method described in Section III to correctly detect a patch of an homogeneous fractal texture characterized by a local Hölder exponent $H_{\mathrm{p}} = 0.5$, mimicking disrupted tissues, immersed in an homogeneous texture background, characterized either by $H_{\mathrm{b}} = 0.3$ to model *fatty* tissues or $H_{\mathrm{b}} = 0.65$ associated to *dense* tissues [5]. The ultimate goal is to provide numerical evidence of the gap in difficulty of Hölder exponent-based breast cancer risk assessment between predominantly *fatty* and predominantly *dense* breasts and to quantify the potential detection bias induced by a difference in surrounding tissue density.

Experimental setup. Following the analyses performed in [4], [5], in which the authors discriminate mammographic tissues based on the local Hurst exponent, two configurations are considered:

- *fatty* background: detection of a patch of disrupted tissues, $H_{\mathrm{p}} = 0.5$, immersed in fatty tissues, $H_{\mathrm{b}} = 0.3$;
- *dense* background: detection of a patch of disrupted tissues, $H_{\mathrm{p}} = 0.5$, immersed in dense tissues, $H_{\mathrm{b}} = 0.65$.

As an illustration, one example of each configuration is provided in Figure 2, with in the first column the ground truth piecewise

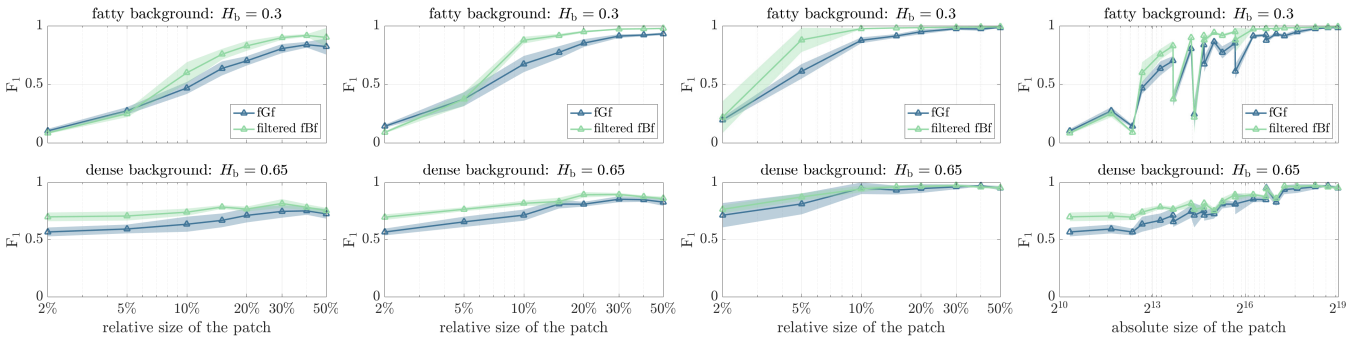

(a) $N = 256$ (b) $N = 512$ (c) $N = 1024$ (d) All resolutions

Fig. 4: **F-score for the detection of a central patch with $H = 0.5$ in fatty vs. dense textured background as a function of the relative (a-c) or absolute (d) size of the patch.** Performance averaged over $R = 10$ realizations with associated 95% Gaussian confidence intervals.

constant local Hölder exponent maps, in the second column the piecewise homogeneous fractional Gaussian field, obtained from Equation (4), and in the third column, piecewise homogeneous filtered fractional Brownian field, resulting from Equation (5). For each of these two configurations, eight *relative* sizes of the circular patch of disrupted tissue to be detected are considered, covering respectively $\{2\%, 5\%, 10\%, 15\%, 20\%, 30\%, 40\%, 50\%\}$ of the whole textured image composed of M pixels. Three image resolutions are considered $N \in \{256, 512, 1024\}$ in order to explore both the influence of the *relative* and *absolute* sizes of the central patch to be detected. Finally, for each configuration, each relative size and each absolute size, $R = 10$ realizations of the fractional Gaussian field and filter fractional Brownian field textures are generated and reported performance are averaged over these R realizations and accompanied by 95% Gaussian confidence regions.

Performance evaluation. To quantity the accuracy of the segmentation of the central patch, modeling disrupted tissues, inside the textured background, modeling fatty or dense tissues, the so-called *F-score* is well adapted. Indeed, it accounts both for the two possible sources of error: first, pixels originally belonging to the *healthy*, fatty or dense, background and second, erroneously classified as *disrupted*, error of type I, and for pixels originally belonging to the patch and erroneously classified as background, error of type II. During segmentation, each pixel is classified either as belonging to the background texture, i.e., consisting in *healthy* tissues, or to the central patch texture, i.e., exhibiting some *disrupted* structure. Let first define the precision and recall associated to such a segmentation:

- precision: proportion of pixels segmented as belonging to the central patch which indeed originally belong to it;
- recall: proportion of pixels originally belonging to the central patch which have been correctly segmented.

Then, the F-score, belonging to $[0, 1]$, is defined as $\mathsf{F}_1^{-1} = \mathsf{precision}^{-1} + \mathsf{recall}^{-1}$. The larger the F-score, the better the segmentation in terms of both errors of types I and II.

Detection performance for different *relative* sizes of the patch. Figure 4 displays the F-score measuring the quality of the two-class segmentation $\mathcal{T}\widehat{h}^{\mathsf{ROF}}$ obtained from the minimization of (9). As expected, one can observe that the accuracy of the segmentation, quantified by the F-score, decreases as the relative size of the patch of disrupted tissue decreases. Further, one can observe that the F-score decreases faster with the relative patch size in the case of *fatty* background, represented in the top row plots of Figure 4 than is the case of *dense* background, in bottom plots. For large patches, detection is easier in *fatty* than in *dense* backgrounds, which is in line with radiologists claim that it is more difficult to detected (pre-)cancerous lesions in *dense* breasts than in *fatty* breasts [37], [38]. Though, as the patch size decreases, it rapidly becomes very difficult to detect disrupted tissues in *fatty* backgrounds, which contrasts with the case of *dense* backgrounds in which the F-score remains larger than 0.5 even for small patches. This observation interestingly complements current knowledge and motivates further analysis of the impact of the lesions size on detectability.

Detectability depending on the *absolute* size of the patch. Figure 4d displays the detection performance, quantified through the F-score, as a function of the *absolute* size of the central patch, counted as the total number of pixels falling into the central disk. Bottom plot of Figure 4d confirms that the detection performance in *dense* backgrounds steadily decrease with the *absolute* patch size, though disrupted tissue patch segmentation can be achieved reasonably well, with F-scores always greater than 0.5, even for very small patches. On the contrary, in the case of *fatty* backgrounds, the F-score is an erratic function of the absolute size as displayed in top plot of Figure 4d. While overall decreasing with the *absolute* patch size, performance shows significant drops, which could be caused by dramatic finite-size effects, demonstrating a dramatic lack of robustness.

Comparison of texture models. Finally, it is worth remarking that all these conclusions apply both to the synthetic textures generated using the fractional Gaussian field model proposed in [24, Section 4] and the novel filtered fractional Brownian field constructed in Equation (5). Yet, in contrast with visual inspection of Figure 1, the filtered fractional Brownian fields seem slightly easier to segment than the fractional Gaussian fields, which shows their complementarity.

V. Conclusion

Systematic numerical experiments on synthetic isotropic textures showed that detectability of disrupted tissues depends both on the quantity of tissues and on their environment in a nontrivial way, providing complementary insights on the role of breast density in cancer risk assessment. Few works have exhibited some cases in which mammograms present anisotropy properties, see e.g., [39], but the subject remains vastly unexplored. A natural and promising extension of the present work is thus to investigate detectability of disrupted tissues in anistropic textures. The overarching goal of this line of research is to provide some confidence level on the accuracy of local Hölder exponent-based risk cancer assessment methodology developed in [4], [16]. To that aim, publicly available mammographic datasets will be then processed with fractal analysis tool, including Digital Database for Screening Mammography[3] and VinDr-Mammo[4].

[3] https://www.cancerimagingarchive.net/collection/cbis-ddsm/
[4] https://www.physionet.org/content/vindr-mammo/1.0.0/

REFERENCES

[1] M. Nielsen, J. Thomsen, S. Primdahl, U. Dyreborg, and J. Andersen, "Breast cancer and atypia among young and middle-aged women: a study of 110 medicolegal autopsies," *British journal of cancer*, vol. 56, no. 6, pp. 814–819, 1987.

[2] R. J. Santen, W. Yue, and D. F. Heitjan, "Occult breast tumor reservoir: biological properties and clinical significance," *Hormones and Cancer*, vol. 4, pp. 195–207, 2013.

[3] N. Houssami, S. Ciatto, F. Martinelli, R. Bonardi, and S. W. Duffy, "Early detection of second breast cancers improves prognosis in breast cancer survivors," *Ann. Oncol.*, vol. 20, no. 9, pp. 1505–1510, 2009.

[4] Z. Marin, K. A. Batchelder, B. C. Toner, L. Guimond, E. Gerasimova-Chechkina, A. R. Harrow, A. Arneodo, and A. Khalil, "Mammographic evidence of microenvironment changes in tumorous breasts," *Medical Physics*, vol. 44, no. 4, pp. 1324–1336, 2017.

[5] P. Kestener, J.-M. Lina, P. Saint-Jean, and A. Arneodo, "Wavelet-based multifractal formalism to assist in diagnosis in digitized mammograms," *Image analysis and stereology*, vol. 20, no. 3, pp. 169–174, 2001.

[6] T. Lundahl, W. J. Ohley, S. M. Kay, and R. Siffert, "Fractional Brownian motion: A maximum likelihood estimator and its application to image texture," *IEEE Trans. Med. Imaging*, vol. 5, no. 3, pp. 152–161, 1986.

[7] C.-L. Benhamou, S. Poupon, E. Lespessailles, S. Loiseau, R. Jennane, V. Siroux, W. Ohley, and L. Pothuaud, "Fractal Analysis of Radiographic Trabecular Bone Texture and Bone Mineral Density: Two Complementary Parameters Related to Osteoporotic Fractures," *J. Bone Miner. Res.*, vol. 16, no. 4, pp. 697–704, 2001.

[8] B. Brunet-Imbault, G. Lemineur, C. Chappard, R. Harba, and C.-L. Benhamou, "A new anisotropy index on trabecular bone radiographic images using the fast Fourier transform," *BMC Med. Imaging*, vol. 5, pp. 1–11, 2005.

[9] J. Cui, C. L. Liu, R. Jennane, S. Ai, K. Dai, and T.-Y. Tsai, "A highly generalized classifier for osteoporosis radiography based on multiscale fractal, lacunarity, and entropy distributions," *Front. Bioeng. Biotechnol.*, vol. 11, p. 1054991, 2023.

[10] Z. Y. Shan, J. Z. Liu, J. O. Glass, A. Gajjar, C.-S. Li, and W. E. Reddick, "Quantitative morphologic evaluation of white matter in survivors of childhood medulloblastoma," *Magn. Reson. imaging*, vol. 24, no. 8, pp. 1015–1022, 2006.

[11] X. Zhuang and Q. Meng, "Local fuzzy fractal dimension and its application in medical image processing," *Art. Intell. Med.*, vol. 32, no. 1, pp. 29–36, 2004.

[12] C. B. Caldwell, S. J. Stapleton, D. W. Holdsworth, R. A. Jong, W. J. Weiser, G. Cooke, and M. J. Yaffe, "Characterisation of mammographic parenchymal pattern by fractal dimension," *Physics in medicine & biology*, vol. 35, no. 2, p. 235, 1990.

[13] A. E. Burgess, F. L. Jacobson, and P. F. Judy, "Human observer detection experiments with mammograms and power-law noise," *Med. Phys.*, vol. 28, no. 4, pp. 419–437, 2001.

[14] B. Grosjean and L. Moisan, "A-contrario detectability of spots in textured backgrounds," *J. Math. Imaging Vis.*, vol. 33, pp. 313–337, 2009.

[15] D. A. Zebari, D. A. Ibrahim, D. Q. Zeebaree, M. A. Mohammed, H. Haron, N. A. Zebari, R. Damaševičius, and R. Maskeliūnas, "Breast cancer detection using mammogram images with improved multi-fractal dimension approach and feature fusion," *Appl. Sci.*, vol. 11, no. 24, p. 12122, 2021.

[16] E. Gerasimova-Chechkina, B. C. Toner, K. A. Batchelder, B. White, G. Freynd, I. Antipev, A. Arneodo, and A. Khalil, "Loss of Mammographic tissue homeostasis in invasive lobular and ductal breast carcinomas vs. benign lesions," *Front. Physiol.*, vol. 12, p. 660883, 2021.

[17] H. Wendt, L. Leon, J.-Y. Tourneret, and P. Abry, "Multifractal anomaly detection in images via space-scale surrogates," in *Proc. IEEE Int. Conf. Image Process.* IEEE, 2022, pp. 556–560.

[18] J. Ilow and H. Leung, "Self-similar texture modeling using FARIMA processes with applications to satellite images," *IEEE Trans. Image Process.*, vol. 10, no. 5, pp. 792–797, 2001.

[19] H. Biermé, F. Richard, M. Rachidi, and C.-L. Benhamou, "Anisotropic texture modeling and applications to medical image analysis," in *Proc. ESAIM*, vol. 26. EDP Sciences, 2009, pp. 100–122.

[20] S. Cohen and J. Istas, *Fractional fields and applications*. Springer, 2013.

[21] R. M. Pereira, C. Garban, and L. Chevillard, "A dissipative random velocity field for fully developed fluid turbulence," *J. Fluid Mech.*, vol. 794, pp. 369–408, 2016.

[22] A. Napolitano, S. Ungania, and V. Cannata, "Fractal dimension estimation methods for biomedical images," *MATLAB—A fundamental tool for scientific computing and engineering applications*, vol. 3, pp. 161–178, 2012.

[23] B. B. Mandelbrot and J. W. Van Ness, "Fractional Brownian motions, fractional noises and applications," *SIAM review*, vol. 10, no. 4, pp. 422–437, 1968.

[24] B. Pascal, N. Pustelnik, and P. Abry, "Strongly Convex Optimization for Joint Fractal Feature Estimation and Texture Segmentation," *Appl. Comput. Harmon. Anal.*, vol. 54, pp. 303–322, 2021. [Online]. Available: https://hal.archives-ouvertes.fr/hal-02346159/document

[25] H. Biermé, P. Carré, C. Lacaux, and C. Launay, "Gaussian Random fields and monogenic images," *Preprint*, 2024. [Online]. Available: https://hal.science/hal-04659825v1/document

[26] S. Mallat, *A wavelet tour of signal processing*. San Diego, USA: Academic Press, 1997.

[27] S. Jaffard, "Wavelet techniques in multifractal analysis," *Fractal Geometry and Applications: A Jubilee of Benoît Mandelbrot, M. Lapidus and M. van Frankenhuijsen Eds., Proceedings of Symposia in Pure Mathematics*, vol. 72, no. 2, pp. 91–152, 2004.

[28] R. Leonarduzzi, H. Wendt, P. Abry, S. Jaffard, C. Melot, S. G. Roux, and M. E. Torres, "p-exponent and p-leaders, Part II: Multifractal Analysis. Relations to Detrended Fluctuation Analysis." *Physica A*, vol. 448, pp. 319–339, 2016. [Online]. Available: http://arxiv.org/pdf/1507.06641v2.pdf

[29] H. Wendt, S. G. Roux, P. Abry, and S. Jaffard, "Wavelet leaders and bootstrap for multifractal analysis of images," *Signal Process.*, vol. 89, no. 6, pp. 1100–1114, 2009.

[30] S. Jaffard, B. Lashermes, and P. Abry, "Wavelet Leaders in Multifractal Analysis," in *Wavelet Analysis and Applications*. Springer, 2007, pp. 201–246.

[31] J. D. B. Nelson, C. Nafornita, and A. Isar, "Semi-local scaling exponent estimation with box-penalty constraints and total-variation regularization," *IEEE Trans. Image Process.*, vol. 25, no. 7, pp. 3167–3181, 2016.

[32] B. Pascal, N. Pustelnik, P. Abry, and J.-C. Pesquet, "Block-coordinate proximal algorithms for scale-free texture segmentation," in *Proc. IEEE Int. Conf. Acoust. Speech Signal Process.* Calgary, Alberta, Canada: IEEE, Apr. 15-20 2018, pp. 1253–1257. [Online]. Available: https://hal.inria.fr/hal-01736991/document

[33] A. Chambolle and T. Pock, "A first-order primal-dual algorithm for convex problems with applications to imaging," *J. Math. Imaging Vis.*, vol. 40, no. 1, pp. 120–145, 2011.

[34] B. Pascal, N. Pustelnik, P. Abry, G. J.-C., and V. Vidal, "Parameter-free and fast nonlinear piecewise filtering: application to experimental physics," *Ann. Telecommun.*, vol. 75, no. 11, pp. 655–671, 2020.

[35] X. Cai and G. Steidl, "Multiclass segmentation by iterated ROF thresholding," in *International Workshop on Energy Minimization Methods in Computer Vision and Pattern Recognition*. Springer, 2013, pp. 237–250.

[36] B. Pascal, S. Vaiter, N. Pustelnik, and P. Abry, "Automated data-driven selection of the hyperparameters for Total-Variation based texture segmentation," *J. Math. Imaging Vis.*, pp. 1–30, 2021. [Online]. Available: https://hal.archives-ouvertes.fr/hal-03044181/document

[37] J. J. Heine and P. Malhotra, "Mammographic tissue, breast cancer risk, serial image analysis, and digital mammography: Part 1. Tissue and related risk factors," *Academic radiology*, vol. 9, no. 3, pp. 298–316, 2002.

[38] A. L. Brown, C. Vijapura, M. Patel, A. De La Cruz, and R. Wahab, "Breast cancer in dense breasts: detection challenges and supplemental screening opportunities," *RadioGraphics*, vol. 43, no. 10, p. e230024, 2023.

[39] F. Richard and H. Bierme, "Statistical tests of anisotropy for fractional Brownian textures. Application to full-field digital mammography," *J. Math. Imaging Vis.*, vol. 36, pp. 227–240, 2010.